

# A Physical Modeling Based Unification Framework for Cone Beam CT Reconstruction

Ti Bai, Xi Chen and Xuanqin Mou

**Abstract**—Data degradations including quantum noise, beam hardening and scatter remain a major issue in preclinical/clinical applications, despite the recent advances in x-ray computed tomography. Substantial efforts have been devoted to address individual degradations, however, little attention has been paid to minimize the adverse effects in a unified fashion. In this paper, we combine image reconstruction and artifact reduction in a physics-based synergistic framework. Simulation results showed that less than 10 HU error could be achieved with the proposed framework. Real data experiments showed that the corrected reconstructions with the proposed method exhibited comparable CT values and noise levels as the associated planning CT images.

**Index Terms**—Reconstruction, cone beam CT, noise, beam hardening, scatter

## I. INTRODUCTION

THE urgent demands of accurate non-destructive sensing on the interior structures of the object have inspired a rapid technical development of x-ray computed tomography in the last decades which has been applied in a wide array of scenarios, such as industrial non-destructive detection, medical diagnostic imaging, image guided radiation therapy/surgery and preclinical small animal imaging. Despite the significant progress made both in the aspects of hardware and algorithm, there still exist substantial flaws heavily impairing the reconstruction qualities stemmed from various data degradations including quantum noise, beam hardening, scatter and so on.

Owing to the inherent stochastic properties of the photon-material interactions, quantum noise in the projection data is inevitable. It would be magnified and propagated to the reconstructed images resulting in streak artifacts and/or reducing the low contrast tissue detectability. Substantial efforts have been devoted to the noise reduction. They basically could be divided into two categories: pre/post-processing methods and model-based iterative methods. A major strategy of the pre/post-processing methods is applying a sophisticated linear or nonlinear filter directly on the projection data/the reconstructed image to weaken the noise[1]. Model-based iterative algorithms formulate the reconstruction tasks into optimization problems by considering the noise's stochastic properties and/or incorporating certain physical constraints[2]. Either Poisson distribution of the raw data before log or Gaussian distribution of the line integral data after log are widely adopted[1], [2]. As for the physical constraints, s-parsity promotion regularizers, such as total variation(TV) minimization[3] and dictionary learning(DL) based sparse representation[4], are popular availing from the compressive sensing techniques.

Rising from the inherent polychromaticity of the x-ray source spectrum, beam hardening effects may potentially lead

This work was supported by the National Natural Science Foundation of China (NSFC) (No. 61571359), the National Key Research and Development Program of China (No. 2016YFA0202003) and the National Natural Science Foundation of China (NSFC) (No. 61401349).

Ti Bai, Xi Chen and Xuanqin Mou are with the Institute of Image processing and Pattern recognition, Xi'an Jiaotong University, Xi'an, Shaanxi, 710049, China. (e-mail: xi\_chen@mail.xjtu.edu.cn, xqmou@mail.xjtu.edu.cn)

to cupping artifacts and dark streak artifacts, rendering the images difficult to be used. An ensemble of studies have been carried out to alleviate this problem, for example, the classical correction method that combines water correction[5] and bone correction[6] together has been used in the commercial x-ray CT systems. A statistical polyenergetic reconstruction framework was also proposed and showed a promising reduction of the beam hardening artifacts[2].

Scatter effects are heavily pronounced when large area detector array presents in an x-ray system, causing contrast loss and severe distortions, such as cupping artifacts, dark streak artifacts and etc[7]. A variety of methods have been devised in literature to enhance the image qualities, such as the hardware-based methods including air-gap, anti-scatter grid, beam stop array, primary modulation[8] and so on. An alternative approach is the software-based method which firstly mathematically estimates the scatter in the projection or image domain[9], and then performs the correction step. The scatter components could be estimated with the Monte Carlo(MC) technique by accurately simulating the photon transportation process[10] or the analytic technique based on a convolution kernel[11]. With the assumption that the attenuation coefficients of the human tissues are known to be relatively stable and uniform, the scatter components could also be estimated iteratively in the image domain[9] or analytically in the projection domain[11].

Many techniques have been proposed in literature to alleviate the above mentioned individual degradation factor. However, to our best knowledge, little attention has been paid to approaching a unified reconstruction framework in terms of that correcting all of these degradation factors in an one-time work. In this study, we attempt to devise such a unified reconstruction framework, where the scatter components could be calculated iteratively while updating the reconstructed images. The relevant theories and the experimental results will be presented in sec. (II) and sec. (III), respectively. In sec. (IV), we will discuss and conclude the whole study.

## II. METHODS AND MATERIALS

### A. Formulation

In this section, we would first introduce the notations. Generally speaking, our task is to calculate the underlying density volume  $\rho$  and the associated scatter component  $s$  simultaneously, provided the raw measurements  $Y$  and that the x-ray spectrum is known. The maximum a posteriori estimation could be formulated as:

$$\begin{aligned} P(\rho, s|Y) &= \frac{P(Y|\rho, s)P(\rho, s)}{P(Y)} \\ &= \frac{\prod_i P(Y_i|\rho, s)P(\rho)P(s)}{P(Y)}, \end{aligned} \quad (1)$$

where  $Y_i$  denotes the real measurement of the  $i$ th ray. Here we assume that the measurements among different detectors

are independent[2]. And it is also supposed that the density volume  $\rho$  and the scatter component  $s$  are independent with each other.

Then the associated cost function could be achieved by performing negative log operation on Eq. (1) as:

$$L(\rho, s) = - \sum_i \log P(Y_i | \rho, s) - \log P(\rho) - \log P(s) + \log P(Y). \quad (2)$$

In this work, we adopt the Poisson model for the raw measurements and also consider a broad spectrum for the polyenergetic source[2], and hence we have:

$$P(Y_i | \rho, s) = \frac{\bar{Y}_i^{Y_i} e^{-\bar{Y}_i}}{Y_i!}, \quad (3)$$

where  $\bar{Y}_i = \sum_e I_i(e) \exp(-\sum_k \sum_j m_{kj}(e) \rho_j l_{ij}) + s_i$  denotes the expected value of the  $i_{\text{th}}$  detector.  $I_i(e)$  and  $s_i$  represent the fluence of photon energy  $e$  and the detected scatter signal.  $l_{ij}$  models the system matrix meaning the length of the intersection between the  $i_{\text{th}}$  ray and the  $j_{\text{th}}$  voxel of the reconstructed volume. Suppose that the reconstructed volume could be classified into  $K$  types of materials. Then, the mass attenuation coefficient of the  $j_{\text{th}}$  voxel under energy  $e$  refers to  $m_{kj}(e)$  if it belongs to the  $k_{\text{th}}$  type material.

Regarding the scatter component  $s$  which is known to be dominated by the extremely low frequency components, it is reasonable to assume that the associated gradient map  $\|\nabla s\|_2$  follows a general Gaussian distribution with precision parameter  $\lambda$  and shape parameter  $p$ , i.e.,

$$P(s) \propto e^{-\lambda \|\nabla s\|_2^p}, \quad (4)$$

where we define the square of the gradient at spatial location  $(x, y, z)$  as:

$$\begin{aligned} (\|\nabla s\|_2^2)_{x,y,z} &= (s_{x,y,z} - s_{x-1,y,z})^2 \\ &+ (s_{x,y,z} - s_{x,y-1,z})^2 \\ &+ (s_{x,y,z} - s_{x,y,z-1})^2. \end{aligned} \quad (5)$$

Suppose that  $\beta R(\rho) = -\log P(\rho)$  represents certain kind of physical constraint about the density volume, substituting Eqs. (3) and (4) into Eq. (2) and ignoring the irrelevant constant terms, we could express the final objective function as:

$$\Phi(\rho, s) = \min_{\rho, s} \sum_i (\bar{Y}_i - Y_i \log(\bar{Y}_i)) + \lambda \|\nabla s\|_2^p + \beta R(\rho). \quad (6)$$

Note that when the scatter component  $s$  is omitted in Eq. (6), the proposed unified reconstruction framework, will be reduced to the classical polyenergetic reconstruction model.

### B. Optimization algorithm

Basically, there exist two different quantum noise sources in the measurements, i.e., either from the primary signal or from the scatter. If the scatter background is first estimated and then subtracted from the measurements, the resulted signal will produce a noise-amplified reconstruction compared to the uncorrected one. Therefore, a powerful prior information about

the reconstructed volume is required for noise suppression. In the work, we adopt the 3D dictionary learning based sparse representation technique as the regularizer[12]. Then the proposed reconstruction framework could be formulated as:

$$\begin{aligned} \min_{\rho, s, \alpha} \sum_i (\bar{Y}_i - Y_i \log(\bar{Y}_i)) + \lambda \|\nabla s\|_2^2 \\ + \beta \sum_t (\|E_t \rho - D \alpha_t\|_2^2 + \nu \|\alpha_t\|_0), \end{aligned} \quad (7)$$

where  $E_t$  denotes the extraction of the  $t_{\text{th}}$  patch.  $\alpha$  is the sparse coefficient on the basis of dictionary  $D$ ,  $\nu$  is the parameter balancing the sparse coding tolerance and the sparsity level described by  $\|\alpha_t\|_0$ . In this work, the adopted distribution for the scatter gradient map is Gaussian distribution, i.e.,  $p = 2$ .

The optimization of Eq. (7) could be carried out alternatively by splitting into the following three sub-problems:

$$\min_{\rho} \sum_i (\bar{Y}_i - Y_i \log(\bar{Y}_i)) + \beta \sum_t \|E_t \rho - D \alpha_t\|_2^2, \quad (8)$$

$$\min_s \sum_i (\bar{Y}_i - Y_i \log(\bar{Y}_i)) + \lambda \|\nabla s\|_2^2, \quad (9)$$

$$\min_{\alpha} \sum_t (\|E_t \rho - D \alpha_t\|_2^2 + \nu \|\alpha_t\|_0). \quad (10)$$

The well-known separable paraboloidal surrogate (SPS) algorithm could be employed to minimize sub-problems (8) and (9). Sub-problem (10) is to find the sparse representation which could be achieved with the orthogonal matching pursuit algorithm.

### C. Algorithm details

In this work, the reconstructed volume  $\rho$  is initialized with the density volume with respect to its FDK reconstruction[13], based on which, the sparse coefficients  $\alpha$  are initialized with the solution of sub-problem (10).

The scatter component could be initialized as follows. It is reasonable to hypothesised that the majority of the densities of the human soft tissues are relatively stable and uniform in terms of that most of them are in the vicinity of water. Therefore, provided the FDK result which is supposed to be contaminated by various degradations including beam hardening, scatter and noise, etc, then set all the density values inside the object support to be  $1.0 \text{g/cm}^3$  corresponding to the water density while keep the rest unchanged, a water surrogate object could be digitally designed. And then, substituting the above obtained object into sub-problem (9), the solution is considered as the initialization of the scatter component  $s$ .

It is noted that problem (7) has multiple solutions, in other words, the estimated scatter  $s$  and the reconstructed density volume  $\rho$  are correlated with each other. Therefore, a direct optimization of Eq. (7) would result in a scatter component  $s$  highly resembling the above initialized one. In order to alleviate this problem, a segmentation trick is required when solving sub-problem (9). Specifically, to maximize the difference between bone and soft tissue, the segmentation

operation is performed based on the associated CT value map which also considers the mass attenuation coefficients. In this work, after we obtain the current reconstructed density volume  $\rho$ , we will segment it according to a predefined curve as indicated in Eq. (11). And then the segmented density map would be fed into Eq. (9) to update the scatter component. Note that  $0.9\text{g}/\text{cm}^3$  and  $1.05\text{g}/\text{cm}^3$  are the standard density values of adipose and muscle according to National Institute of Standards and Technology (NIST)[14]. And we set  $\rho = 1.0\text{g}/\text{cm}^3$  for those CT values ranging from -50 to 0 to explain the uncertainty about the tissue categories.

$$f(\rho) = \begin{cases} \rho & \text{CT value} < -500 \\ 0.9 & -500 \leq \text{CT value} < -50 \\ 1.0 & -50 \leq \text{CT value} < 0 \\ 1.05 & 0 \leq \text{CT value} < 250 \\ \rho & 250 < \text{CT value} \end{cases} \quad (11)$$

#### D. Experiments

A digital water phantom was fed into the gDRR software package[15] for the projections generation with the scatter contaminated. As illustrated in Fig. (1), to simulate the high attenuated objects, three cylinders with density of  $1.35\text{g}/\text{cm}^3$  and one cylinder with density of  $2.16\text{g}/\text{cm}^3$  are also inserted into the lower-half part of the digital phantom. The radius of the water insert and the four high attenuated cylinders are 10cm and 1.25cm, respectively. A typical system geometry simulating the on board imager (OBI) mounted on a Varian TrueBeam medical accelerator (Varian Medical System, Palo Alto, CA) was employed, where the imager dimension is  $512 \times 384$  with a resolution of  $0.0776 \times 0.0776\text{cm}^2$ . The distances from the source to the isocenter and to the detector are 100cm and 150cm, respectively. For this digital phantom, 360 projections were generated with the full-fan mode in a complete circle, the employed polyenergetic source spectrum has a 100kVp. To collaborate the above simulated case, a real data set containing 656 projections with respect to a prostate patient was also collected with the above OBI in the half-fan mode, i.e., having a 16cm lateral detector shift. The reconstructed volumes are of dimension  $512 \times 512 \times 448$  with a voxel size of  $0.05^3\text{cm}^3$  and of dimension  $512 \times 512 \times 256$  with a voxel size of  $0.1^3\text{cm}^3$ , corresponding to the digital phantom and the prostate patient, respectively.

Once the FDK reconstruction is achieved,  $\rho$ ,  $s$  and  $\alpha$  will be initialized as stated in sec. (II-C). For quantitative comparison, the averaged CT value and the standard deviation(STD) will be calculated based on selected region of interest (ROI).

### III. RESULTS

Figure (2) shows the results of the digital phantom case. Obvious cupping artifacts due to scatter and beam hardening effects could be observed from Fig. (2)(a2), in addition, one also could find the ring artifacts resulted from the high scatter-primary-ratio (SPR) in the bow-tie filter shadow region. When there exist high attenuated objects along the ray path, the artifacts would be more severe, as shown by

TABLE I  
AVERAGED CT VALUES OF THE SELECTED SEVEN ROIS OF THE DIGITAL PHANTOM CASE.(UNIT: HU)

| ROI #             | 1   | 2   | 3   | 4    | 5    | 6   | 7    |
|-------------------|-----|-----|-----|------|------|-----|------|
| ground truth      | 0   | 0   | 0   | 2231 | 0    | 0   | 1016 |
| before correction | -29 | -65 | -39 | 1347 | -132 | -48 | 736  |
| after correction  | -2  | -3  | -3  | 2072 | -8   | -4  | 959  |

TABLE II  
ROI STATISTICS OF THE PROSTATE PATIENT CASE. THE NUMBERS INSIDE THE PARENTHESES ARE THE STANDARD DEVIATIONS(UNIT: HU)

| ROI #             | 1       | 2        | 3        |
|-------------------|---------|----------|----------|
| planning CT       | 63(16)  | 43(17)   | -77(38)  |
| before correction | -77(35) | -179(33) | -230(38) |
| after correction  | 62(17)  | 48(17)   | -105(23) |

the dark streak artifacts in Fig. (2)(b2). With the proposed framework, the artifacts were dramatically alleviated, as shown in Figs. (2)(a3) and (b3). Figures (2)(a4) and (b4) plot the profiles in Figs. (2)(a1) and (b1). It can be found that after correction, the profiles consistently match the ground truth well. To quantitatively evaluate the proposed framework, seven ROIs were selected for the CT value accuracy evaluation, as shown in Fig. (2), whose values were tabulated in Table (I). It was shown that for the water part, the proposed framework could reduce the CT value error to less than 10, and for the high attenuated objects, the CT value accuracy could also be improved significantly.

Figure (3) demonstrated the experimental results of the prostate patient case. Severe scatter artifacts, such as the ring artifact resulted from the bow-tie filter and the black-hole artifact resulted from the half-fan detector shift geometry[16], could be observed from the reconstruction when no correction algorithm is applied, as depicted in Fig. (3)(b). After correction, the overall accuracy of the CT values has been improved remarkably, as shown in Fig. (3)(c). It can be seen that with the proposed framework, substantial scatter artifacts are suppressed dramatically while the noise are also removed efficiently. Quantitative evaluations about the averaged CT values and the standard deviations are carried out based on three different ROIs annotated in the rectangles in Fig. (3), as summarized in Table (II). It could be seen that the CT value accuracy is improved substantially while the noise level is comparable with the planning CT.

### IV. DISCUSSION AND CONCLUSION

In this study, promising reconstructions exhibiting significant artifacts suppression and dramatic noise reduction were achieved with the proposed framework.

High computational burden is one of the main bottlenecks of iterative reconstruction algorithms to be practically used. And some data correction algorithms such as those MC calculation based aggravate this situation. In contrast, in this work, all the dominant data degradations including noise, beam hardening and scatter, are incorporated into a unified framework, and only one extra forward projection is required in each iteration compared to the conventional iterative reconstruction algorithm. This promises added-on value to the practically relevant situations regarding the computation complexity. Besides, in this

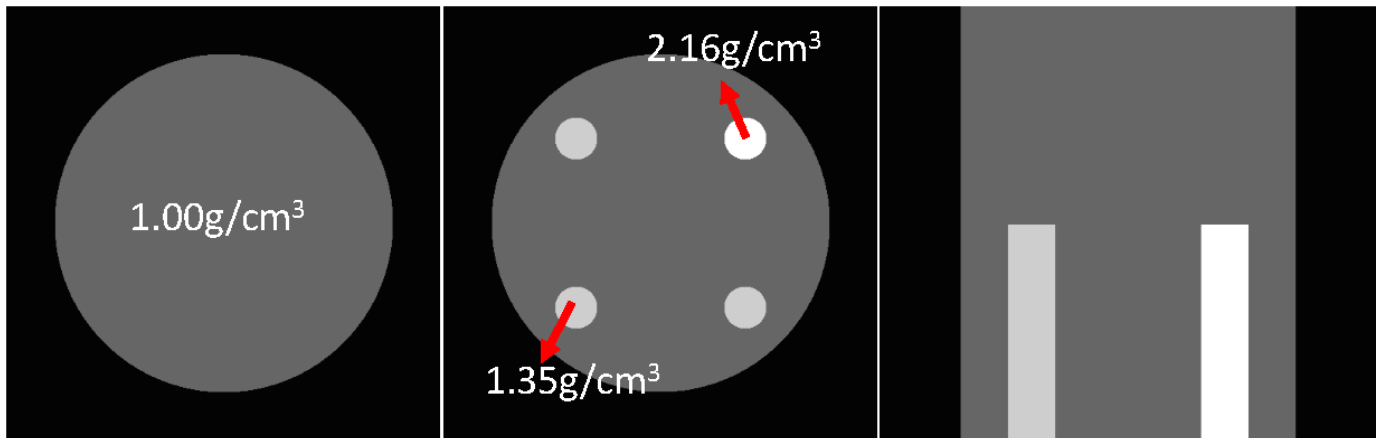


Fig. 1. Digital phantom. The first and the second sub-figures correspond to two different transversal slices, respectively. The third sub-figure displays the coronal view of the phantom. Display window:  $[0 \ 1.65]g/cm^3$ .

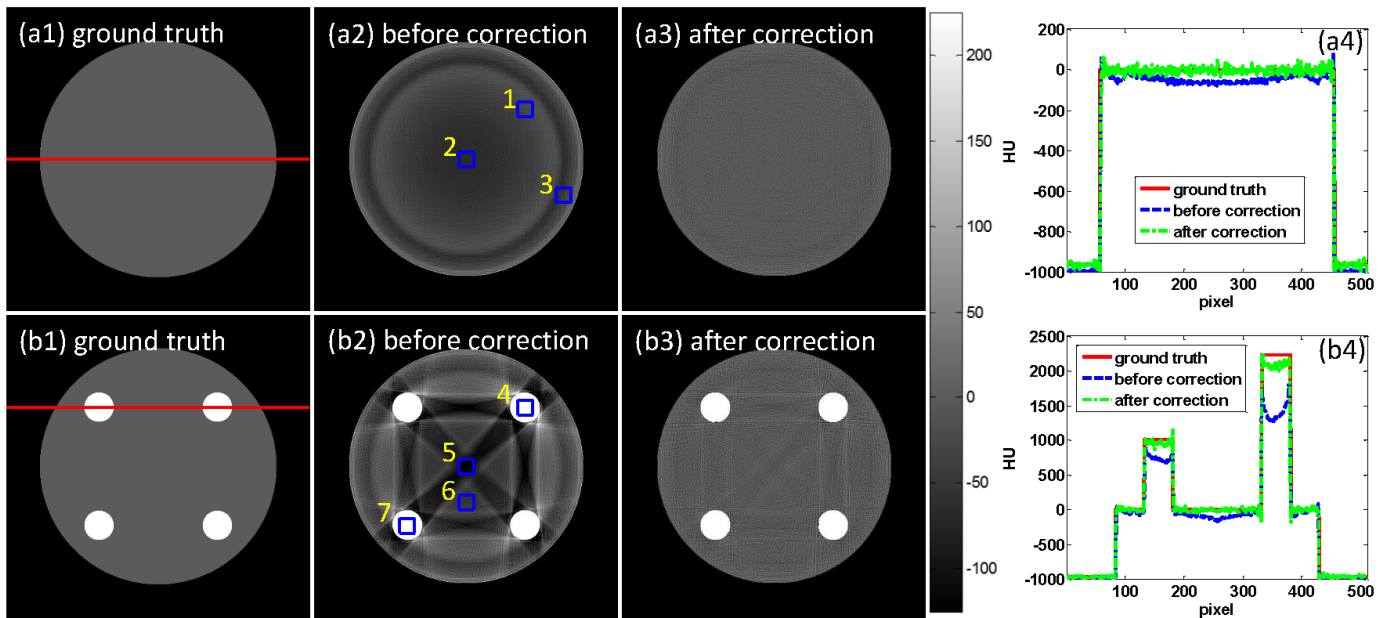


Fig. 2. Correction results for the digital phantom case. Rows (a) and (b) correspond to two different transversal slices. From left to right: images of the ground truth, before correction and after correction. Seven ROIs as indicated by the blue rectangles are selected to calculate the CT values. The fourth column plots the profiles shown in the first column. Display window:  $[-125 \ 225] \text{ HU}$ .

work, to boost the computation performance, several tricks are utilized, such as the order subsets acceleration technique and the Nesterov's momentum technique. Note that both of them are highly parallelizable, and hence, the computation speed can be further enhanced through streamlining its implementation with graphic processing unit(GPU).

Compared to our previous work in CT meeting 2016[17], in this paper, we have conducted several other improvements. In our previous work, we mainly focused on the scatter correction performance, and hence did not take the stochastic property and polyenergetic spectrum into consideration. In this work, all of the three degradation factors were physically modeled, as demonstrated in Eq. (6). Besides, because the effective monoenergetic source was considered in our previous work, the constant consumption of the human soft tissue can only be made based on the linear attenuation coefficients which were correlated with the assumed effective energy. While in this work the polyenergetic spectrum was incorporated, the

assumption could be made based on the density of the tissue which is fixed across different energy channels. Therefore, our newly improved framework would be more realistic and robust.

As there were only one simulated data set and one real data set from IGRT examined in this feasibility study, more detailed comparative studies are necessary to explore the extent to which the proposed framework can be applied, especially in different application scenarios such as small animal imaging, dental CBCT imaging and etc.

In conclusion, a physics-based synergistic reconstruction framework that considers various degradations simultaneously was proposed in this work. Substantial image quality enhancements were achieved with the proposed framework. In the simulated experiment, the proposed framework could reduce the CT value error to less than 10 for the water part, and the CT value accuracy also can be improved significantly for the high attenuated objects. In the real data experiment, comparable

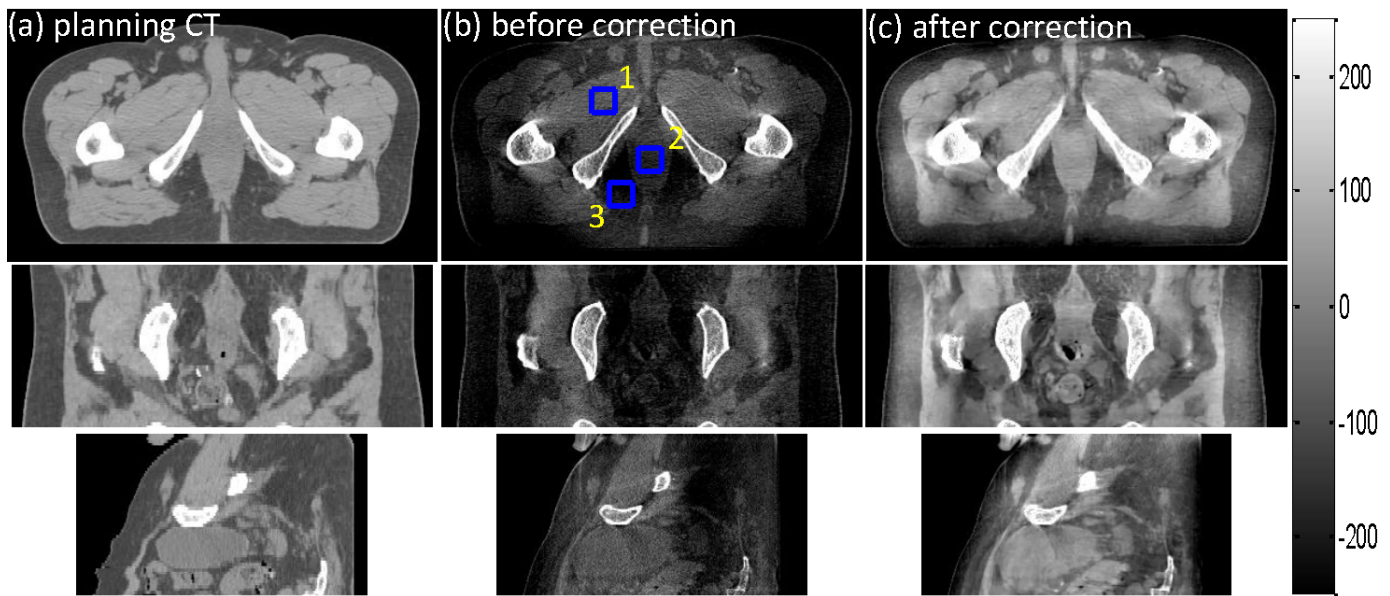


Fig. 3. Correction results for the prostate patient case. (a) (c) correspond to the images of the planning CT, before correction and after correction, respectively. Three ROIs as indicated by the blue rectangles in the middle column are selected to calculate the CT values. Display window: [-250 250] HU.

CT values and noise levels as the planning CT images were achieved with the proposed framework.

#### REFERENCES

- [1] J. Wang, T. Li, H. Lu, and Z. Liang, "Penalized weighted least-squares approach to sinogram noise reduction and image reconstruction for low-dose x-ray computed tomography," *Medical Imaging, IEEE Transactions on*, vol. 25, no. 10, pp. 1272–1283, 2006.
- [2] I. A. Elbakri and J. A. Fessler, "Statistical image reconstruction for polyenergetic x-ray computed tomography," *Medical Imaging IEEE Transactions on*, vol. 21, no. 2, pp. 89 – 99, 2002.
- [3] E. Sidky and X. Pan, "Image reconstruction in circular cone-beam computed tomography by constrained, total-variation minimization," *Physics in medicine and biology*, vol. 53, no. 17, p. 4777, 2008.
- [4] Q. Xu, H. Yu, X. Mou, L. Zhang, J. Hsieh, and G. Wang, "Low-dose x-ray ct reconstruction via dictionary learning," *Medical Imaging, IEEE Transactions on*, vol. 31, no. 9, pp. 1682–1697, 2012.
- [5] W. D. McDavid, R. G. Waggenger, W. H. Payne, and M. J. Dennis, "Correction for spectral artifacts in cross-sectional reconstruction from x rays," *Medical Physics*, vol. 4, no. 1, pp. 54–57, 1977.
- [6] P. M. Joseph and R. D. Spital, "A method for correcting bone induced artifacts in computed tomography scanners," *Journal of Computer Assisted Tomography*, vol. 2, no. 2, pp. 100–8, 1978.
- [7] J. H. Siewerdsen and D. A. Jaffray, "Cone-beam computed tomography with a flat-panel imager: Magnitude and effects of x-ray scatter," *Medical Physics*, vol. 28, no. 2, pp. 220–231, 2001.
- [8] L. Zhu, N. R. Bennett, and R. Fahrig, "Scatter correction method for x-ray ct using primary modulation: Theory and preliminary results," *Medical Imaging, IEEE Transactions on*, vol. 25, no. 12, pp. 1573–1587, 2006.
- [9] P. Wu, X. Sun, H. Hu, T. Mao, W. Zhao, K. Sheng, A. A. Cheung, and T. Niu, "Iterative ct shading correction with no prior information," *Physics in Medicine and Biology*, vol. 60, no. 21, p. 8437, 2015.
- [10] Y. Xu, T. Bai, H. Yan, L. Ouyang, A. Pompos, J. Wang, L. Zhou, S. B. Jiang, and X. Jia, "A practical cone-beam ct scatter correction method with optimized monte carlo simulations for image-guided radiation therapy," *Physics in Medicine & Biology*, vol. 60, no. 9, pp. 3567–3587, 2015.
- [11] W. Zhao, S. Brunner, K. Niu, S. Schafer, K. Royalty, and G. H. Chen, "Patient-specific scatter correction for flat-panel detector-based cone-beam ct imaging," *Physics in Medicine & Biology*, vol. 60, no. 3, pp. 1339–1365(27), 2015.
- [12] T. Bai, H. Yan, F. Shi, X. Jia, Y. Lou, Q. Xu, S. B. Jiang, and X. Mou, "We-g-18a-04: 3d dictionary learning based statistical iterative reconstruction for low-dose cone beam ct imaging," *Medical Physics*, vol. 41, no. 6, pp. 527–527, 2014.
- [13] L. Feldkamp, L. Davis, and J. Kress, "Practical cone-beam algorithm," *JOSA A*, vol. 1, no. 6, pp. 612–619, 1984.
- [14] [Online]. Available: <http://physics.nist.gov/PhysRefData/XrayMassCoef/tab2.html>
- [15] X. Jia, H. Yan, L. Cervino, M. Folkerts, and S. B. Jiang, "A gpu tool for efficient, accurate, and realistic simulation of cone beam ct projections," *Medical Physics*, vol. 39, no. 12, pp. 7368–7378, 2012.
- [16] M. Sun, T. Nagy, G. Virshup, L. Partain, M. Oelhafen, and J. Star-Lack, "Correction for patient table-induced scattered radiation in cone-beam computed tomography (cbct(a)),," *Medical Physics*, vol. 38, no. 4, pp. 2058–2073, 2011.
- [17] H. Y. H. Y. Ti Bai, Xuanqin Mou and G. Wang, "A unified x-ray computed tomographic reconstruction framework," in *The 4th International Conference on Image Formation in X-Ray Computed Tomography*, 2016, pp. 165–168.